Accepted Manuscript

Wheel–rail impact loads and noise generated at railway crossings – Influence of vehicle speed and crossing dip angle

P.T. Torstensson, G. Squicciarini, M. Krüger, B.A. Pålsson, J.C.O. Nielsen, D.J. Thompson

PII: S0022-460X(19)30253-6

DOI: https://doi.org/10.1016/j.jsv.2019.04.034

Reference: YJSVI 14733

To appear in: *Journal of Sound and Vibration*

Received Date: 4 July 2018

Revised Date: 25 April 2019

Accepted Date: 26 April 2019

Please cite this article as: P.T. Torstensson, G. Squicciarini, M. Krüger, B.A. Pålsson, J.C.O. Nielsen, D.J. Thompson, Wheel–rail impact loads and noise generated at railway crossings – Influence of vehicle speed and crossing dip angle, *Journal of Sound and Vibration* (2019), doi: https://doi.org/10.1016/j.jsv.2019.04.034.

Wheel–rail impact loads and noise generated at railway crossings – influence of vehicle speed and crossing dip angle

P.T. Torstensson[1], G. Squicciarini[2], M. Krüger[3], B.A. Pålsson[4], J.C.O. Nielsen[4], D.J. Thompson[2]

[1] Driving Simulation and Visualization, Swedish National Road and Transport Research Institute, SE-402 78 Gothenburg, Sweden

[2] Institute of Sound and Vibration Research, University of Southampton, University Road, Southampton SO17 1BJ, UK

[3] DB Netz AG, Völckerstrasse 5, 80939 Munich, Germany

[4] Department of Mechanics and Maritime Sciences / CHARMEC, Chalmers University of Technology, SE-412 96 Gothenburg, Sweden

Abstract

Wheel–rail impact loads and noise at railway crossings are calculated by applying a hybrid prediction model. It combines the simulation of non-linear vertical dynamic vehicle–track interaction in the time domain and the prediction of sound pressure level using a linear frequency-domain model. The two models are coupled based on the concept of an equivalent roughness spectrum. The time-domain model uses moving Green's functions for the linear vehicle and track models, accounting for wheel structural flexibility and a discretely supported rail with spatially-varying beam properties, and a non-Hertzian wheel–rail contact model. Three-dimensional surface geometry of the wheel and crossing is accounted for in the solution of the wheel–rail contact. The hybrid model is compared against field measurements and is demonstrated by investigating the influence of vehicle speed and crossing geometry on the radiated impact noise. Based on simulation results, it is concluded that the impact loads and noise can be mitigated by reducing the effective dip angle at the crossing, which is determined by the vertical trajectory of the wheel when making the transition between wing rail and crossing nose.

1 Introduction

Turnouts (switches and crossings, S&C) represent components of rail networks that have a large influence on costs. For example, one third of the total maintenance cost for one high-speed line of the Deutsche Bahn (DB), comprising 458 turnouts and carrying an annual traffic load of about 17.5 MGT, was found to be related to the S&C [1]. Wheel–rail impact loads generated on the crossings are causing plastic material flow and rolling contact fatigue damage that may lead to breaking out of pieces of material or even rail fracture. An additional associated issue often overlooked in literature is the radiation of impact noise [2].

There are several turnout configurations to fulfil the needs of various traffic situations. A common layout design is illustrated in Figure 1. It features a straight section called the through route and a curved deviating part referred to as the diverging route. The front of the turnout is defined as the start position of the deviating curve in the switch panel. The switching function is

accomplished by switching machines or actuators that position the switch rails according to the desired traffic route. The closure panel connects the switch and crossing panels, while the crossing panel allows for wheels to travel along both intersecting paths. In a fixed crossing, the wheels need to pass over a gap between wing rail and crossing rail, see description below. This gap can be avoided by a movable (swingnose) crossing, which is a common solution in high-speed lines. Traffic from the switch panel towards the crossing panel is referred to as traffic in the facing move, while the opposite direction is the trailing move. The Theoretical Crossing Point (TCP) in a fixed crossing is where the two gauge faces of the blunt crossing nose would intersect.

The passage of a railway wheel through a fixed crossing in trailing move is illustrated in Figure 2. The gradual decrease in height of the crossing nose results in a downwards motion of the wheel as it travels along the crossing panel. This vertical wheel trajectory is reversed when the wheel makes the transition from the crossing nose to the outwards deviating wing rail. Here, the dynamic vehicle–track interaction typically results in an impact load on the wing rail causing the wheel to accelerate upwards during its continued travel along the wing rail. Several studies have considered design optimisation by longitudinal and transverse re-profiling of the crossing rails as a means to reduce impact loads and damage, see e.g. [3, 4]. The importance of accounting for the substantial variation in (worn) wheel profiles occurring in traffic when modifying the rail design is demonstrated for example in [5].

By combining laboratory measurements on a scale-model and full-scale field measurements with mathematical modelling, Vér et al. [6] presented an extensive investigation of impact noise generated at rail joints. For cases where there is no loss of wheel–rail contact during the passage of a wheel over a rail joint, it was concluded that (1) the static axle load does not influence the radiated impact noise level, and (2) the peak sound pressure level varies with vehicle speed V approximately at a rate of $20\log_{10}(V)$. This relation was confirmed for varying height differences across the rail joint, and more recently it has been verified numerically for the case of impact noise generated by rail joints and wheel flats [7, 8]. For conditions resulting in a short period of loss of wheel–rail contact, the radiated noise was found to approach a constant level independent of speed. Impact noise generated at a step-down rail joint was investigated using a 1:8 experimental scale model in [6]. The peak impact noise level was found to increase with step-down height difference h as $10\log_{10}(h)$.

A numerical method for the prediction of impact noise using a so-called hybrid approach has been presented by Wu and Thompson, see [8]. According to the method, the simulations are performed in two steps: (1) calculation of wheel–rail impact load by a time-domain simulation of non-linear high-frequency vertical dynamic vehicle–track interaction, and (2) prediction of noise using the software TWINS [9] in the frequency domain based on excitation by an equivalent roughness spectrum. In the current work, this approach is applied to investigate impact noise generated at crossings. The paper starts by illustrating the effects of wheel–rail impact at crossings by presenting field measurement data. Thereafter, numerical prediction is applied to investigate the influence of crossing panel surface geometry and vehicle speed on the radiated impact noise level.

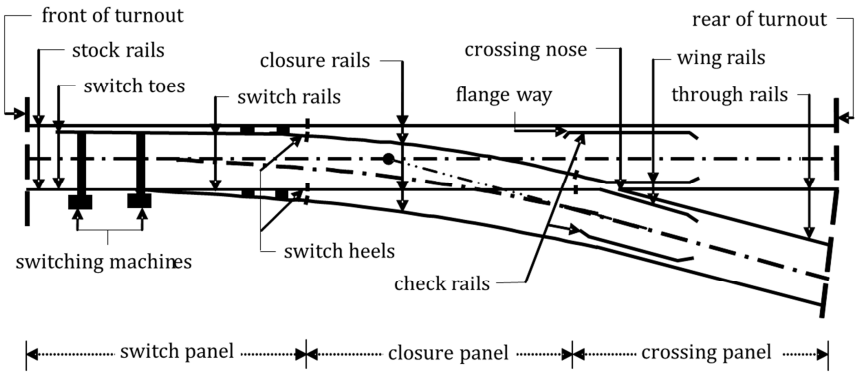

Figure 1. Schematic illustration of a railway turnout and its components

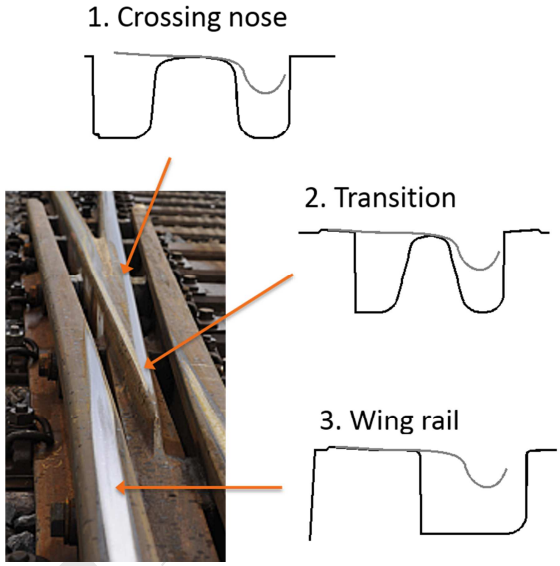

Figure 2. Wheel–rail contact through a fixed crossing illustrated at three instances when the wheel is in: (1) contact with the crossing nose, (2) simultaneous contact with wing rail and crossing nose, and (3) contact with one of the two wing rails. The order of the figures is given for traffic in the trailing move

2 Field measurements

Noise and rail acceleration generated by passenger trains through a fixed crossing in the trailing move have been measured close to the village of Loreley in Germany, see Figure 3. The site is located on the Rhine-Alpine freight corridor with approximately 350 train passages per day. For comparison with the simulation model used in this study, impact tests and pass-by noise and vibration measurements were performed. To calibrate the track model, point and transfer mobilities were measured in the vertical direction along the wing rail and the stock rail in front of the crossing. To record noise and vibration during pass-by, a microphone was set at 7.5 m from the track centre and 1.2 m above the top of rail. The acceleration was recorded in the vertical direction using a 10 mv/g ICP accelerometer adhered centrally to the underside of the wing rail.

The longitudinal position of the sensor was at the end of the running band on the crossing nose, i.e. just before the wheels transition to the wing rail (180 mm from the TCP).

For this study, pass-bys were only recorded for passenger trains. Based on the wheel base (2.6 m) and the time between the two corresponding impacts, the speeds of the trains were estimated to be between 82 and 87 km/h. The train configuration includes four cars and the total number of axles in one train is 10.

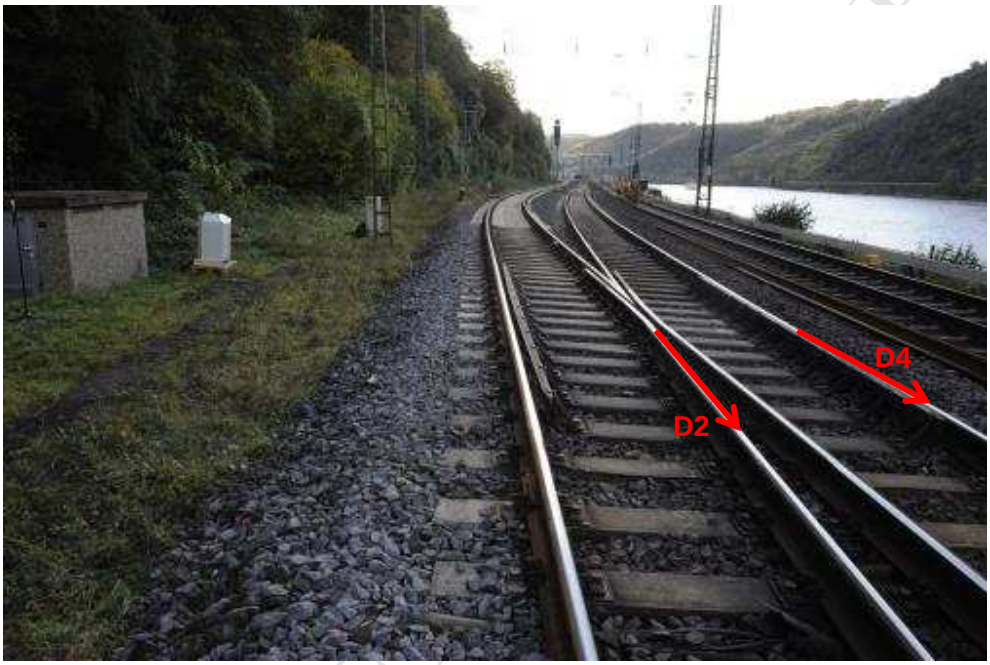

Figure 3. Crossing impact noise measurement site located close to Loreley in Germany. The direction of traffic is in the trailing move along rails D2 and D4. The location of the turnout is in a 500 m radius curve

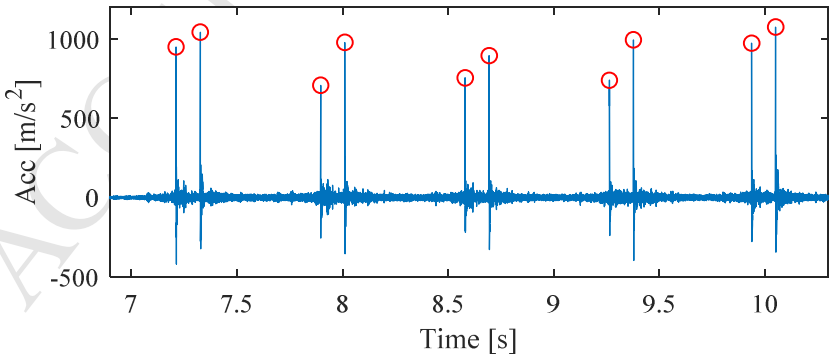

Figure 4. Measured vertical acceleration of the wing rail

Figure 4 shows an example of time history data measured for one of the passenger trains. The impacts can be easily observed in the acceleration data (see circles). However, although clearly audible, these impacts were found to be less evident in the sound pressure signal. To demonstrate

this, the spectrograms of the measured rail velocity and the A-weighted sound pressure are shown in Figures 5(a,b). In the vibration data, the spectrogram is mainly characterised by horizontal bands. These correspond to the impacts and cause the rail to vibrate in a wide frequency range, with most of the energy concentrated between 20 and 1000 Hz. In contrast, the sound pressure spectrogram is mainly characterised by vertical bands. These are caused by the wheel/rail roughness and correspond to the rolling noise. In particular, the two bands at around 400 Hz and 600 Hz stand out noticeably and are likely to be dominating the overall levels. The boundaries of these bands are represented in Figure 5(b) with vertical dashed lines.

A one-third octave band analysis was also performed on the signals. The pass-by time history was divided into five different time windows. Each time window included two wheelsets at its centre and corresponded to the length of a single car. Both velocity and sound pressure levels are shown in Figure 6. The velocity data shows a broad peak centred at 63 – 80 Hz, corresponding to a resonance of the coupled wheel–track system. The lines corresponding to the first and last bogies are above the others as the impact on these wheels is higher (see Figure 4). The noise spectra in Figure 6(b) are found to be consistent for the different windows for frequencies below 2 kHz. At higher frequencies, the spectra corresponding to the first two bogies are 5 – 7 dB above the others, but this is believed to be due to traction noise or to a different roughness on the leading wheels as there was no evidence in the track vibration signals to relate this to the impacts. The sound pressure has two significant peaks at 400 and 630 Hz which are due to rail roughness (see below)

The spectra shown in Figure 6(b) include the summed contributions of rolling noise and impact noise, and it is not possible to separate them completely. The only common feature between the vibration and noise spectra is the broad peak at 63 – 80 Hz. It is possible therefore that this is the main contribution of the impacts on the third octave band spectrum calculated over the length of a car. In general however, based on the analysis shown in Figures 5 and 6, it can only be inferred that the contribution of the impact noise to the sound pressure spectra was small.

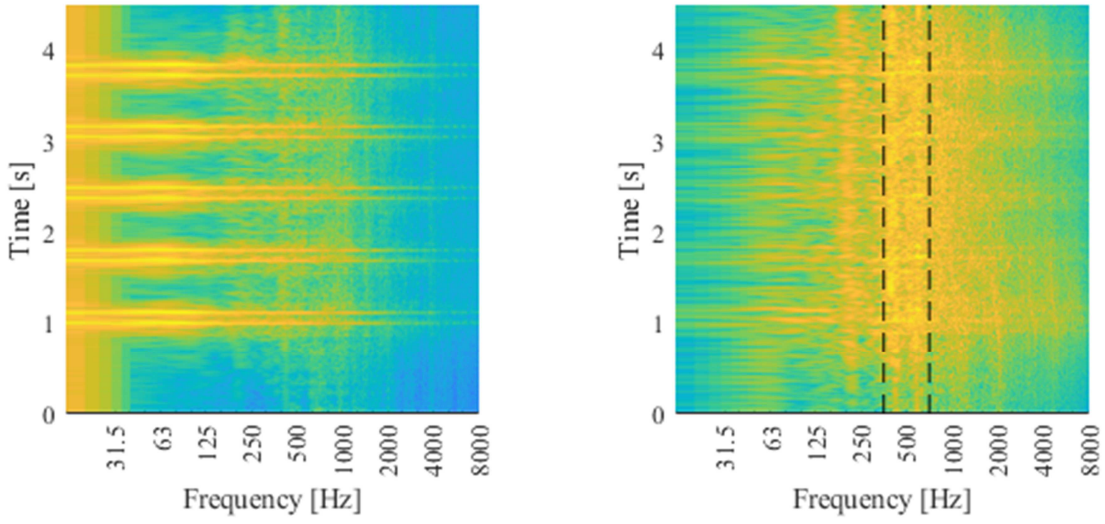

(a) (b)

Figure 5. Measured (a) rail vibration level and (b) sound pressure level spectrograms

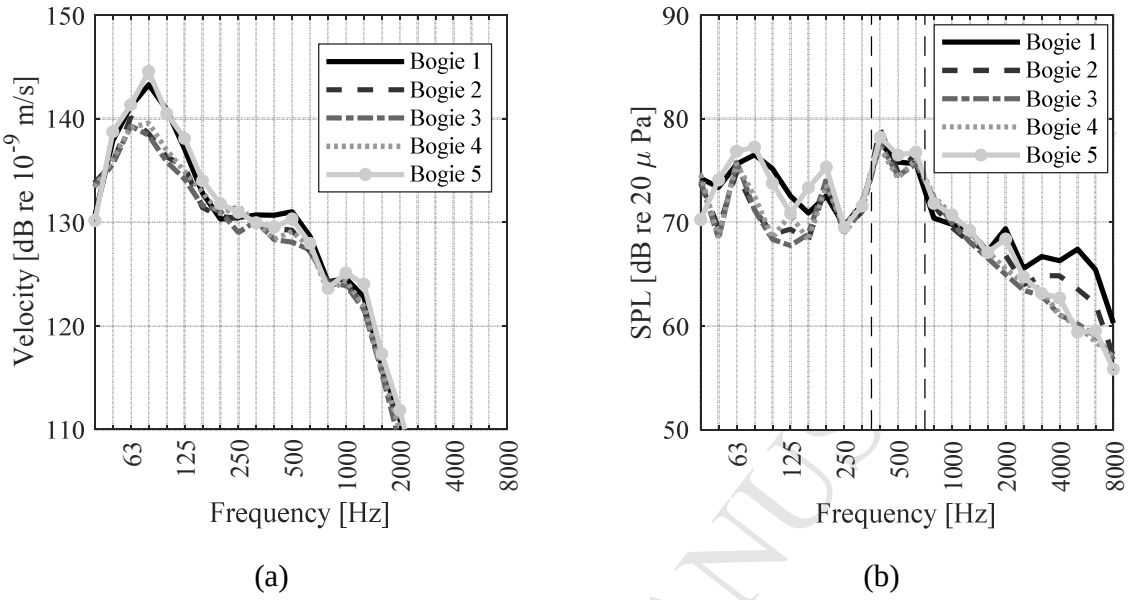

(a) (b)

Figure 6. Measured (a) rail vibration levels and (b) sound pressure levels for the different cars

3 Excitation by crossing panel surface geometry

The geometry of the running surface of the crossing panel was measured using a hand-held 3D laser scanner [10]. The resolution and accuracy of the equipment are 50 μm and ± 30 μm, respectively. Figure 7 shows the measured raw data together with the extracted rail profiles. A computer program that reads and orientates the data, identifies the location of the TCP and extracts rail profiles at a given sampling distance was developed in the software Matlab. At each time step of the simulations of dynamic vehicle–turnout interaction (see Section 4), the three-dimensional crossing contact geometry is obtained by interpolation between these extracted rail profiles. The rail profiles were extracted at a sampling distance of 10 mm.

The rail roughness was measured in front of the crossing using a Corrugation Analysis Trolley (CAT) [11], see Figures 3 and 8. The roughness was measured over 26 m on the wing rail (line D2 in Figure 3) starting from the crossing and moving the CAT in the direction of the traffic. For the stock rail, the distance covered with the CAT was about 40 m, with roughly 20 m on each side of the point corresponding to the crossing noise. It is observed that the roughness on the wing rail (D2) exceeded the ISO 3095 spectrum for wavelengths shorter than 8 cm. It is possible that this is due to the limited access of grinding machinery to this part of the rail. As a consequence, rolling noise will increase while travelling through the crossing. Based on Figures 6(b) and 8, the high roughness level on rail D2 at wavelengths in the interval 3 – 6 cm is the reason for the observed peaks in the sound level spectra at 400 Hz and 630 Hz (measured at vehicle speeds in the range 82 – 87 km/h). To demonstrate this, the lower and upper limits of the frequency bands centered at 400 and 630 Hz are represented by the vertical dashed lines in Figure

6(b) and converted to the corresponding wavelength (λ) range in Figure 8 through the relation $f = v/\lambda$. A speed, v, of 82 km/h is assumed in this case.

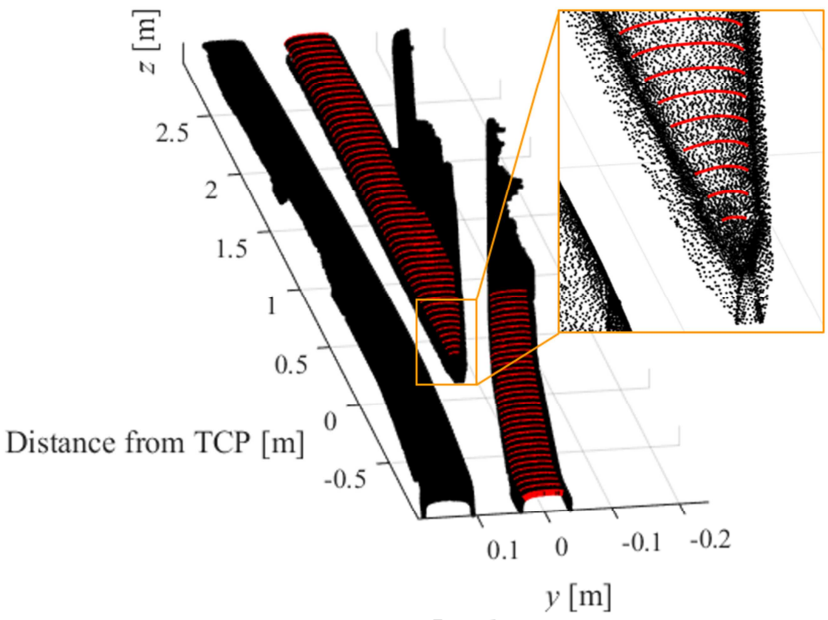

Figure 7. Crossing panel geometry at Loreley measured with a hand-held scanning equipment (black dots). Extracted rail profiles are shown in red

The simulation method proposed in the current paper has previously been applied to investigate the influence of the wheel profile state of wear on the impact noise generated at railway crossings [12]. For a case with vehicle speed 100 km/h and a hollow worn wheel, leading to loss of wheel–rail contact during the transition from wing rail to the crossing nose, the predicted noise level was 11 dB(A) higher than that of a nominal S1002 wheel profile. The state of the wheels fitted on the trains recorded in the measurement campaign is unknown and represents a potential error source in this study. Further numerical studies would be required to investigate the influence of the state of the wheel profiles to understand their effects on the generated impact noise.

The vertical position of the wheel centre relative to the rail centre line (i.e. the wheel vertical trajectory) varies as it travels over a fixed crossing (see Figure 2 and 9). Most significantly it changes from a downwards motion to an upwards motion as it makes the transition from wing rail to crossing nose. This change in direction can be modelled using the concept of a dip angle α as defined in Figure 10. The impulse applied to the wheel to achieve this change in direction is proportional to the change in vertical wheel speed which in turn is proportional to the line speed and the dip angle. It is therefore to be expected that the impact loading on a crossing is proportional to the line speed and the dip angle. The dip angle is in turn determined by the crossing geometry and the lateral position and profile geometry of the passing wheel [13].

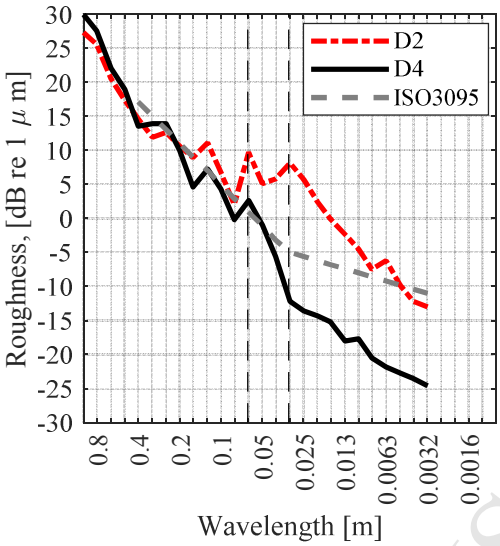

Figure 8. Measured rail roughness spectra for wing rail (D2) and stock rail (D4)

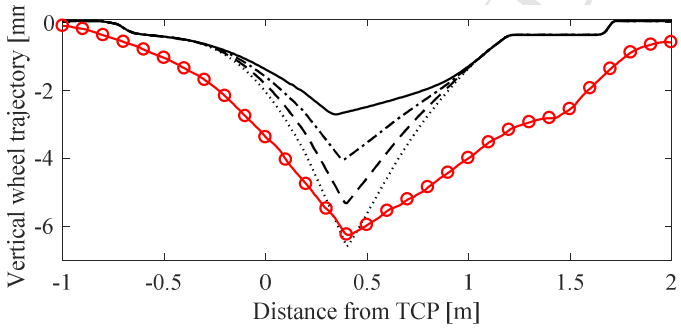

Figure 9. Quasi-static vertical wheel trajectories during pass-by of a S1002 wheel profile on the measured Loreley crossing geometry (—o—), and on generic crossings with dip angle 6 mrad (——), 12 mrad (–·–·–), 18 mrad (– – –) and 24 mrad (·····). Zero relative lateral wheel–rail displacement is assumed

It has been demonstrated experimentally [14, 15] and numerically [16] that geometry change in the transition zone of the crossing due to damage, especially plastic deformation, will influence the wheel–rail interaction and increase the impact loading. These studies have however not reported explicit numbers on changes in dip angles. In [14], acceleration measurements from the same crossing at three different states of degradation are reported. It is shown that the maximum vertical crossing acceleration for a number of passing wheel profiles is on average 70% higher when the crossing is in a damaged state with visible rolling contact fatigue cracks compared to a crossing that has just been maintained to restore the nominal crossing geometry. Everything else being equal, the increase in acceleration indicates a corresponding increase in impact loading and therefore also in dip angle. It is also shown that the longitudinal wheel positions where the maximum vertical accelerations are recorded become more localised in the transition zone for the damaged crossing geometry. As a shorter effective transition zone implies larger dip angles for a given range of wheel profiles [17], it is further evidence that the dip angles for passing wheels have increased with crossing degradation. For the present study, it is assumed that the average dip angle of a damaged crossing could reasonably be twice that of the nominal geometry.

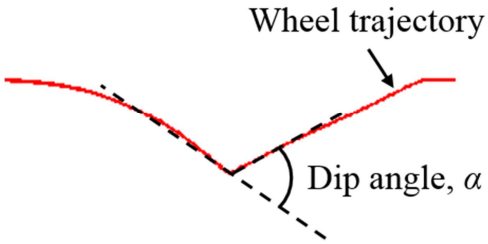

Figure 10. Estimation of effective dip angle based on calculated vertical wheel trajectory (—)

In [17], the average dip angle for 400 measured wheel profiles on a nominal 1:15 crossing was 6.8 mrad with most wheels exhibiting a dip angle between 5 and 10 mrad. These values are for zero lateral wheelset displacement. This variation can be much larger if the lateral displacement is considered [13]. Assuming the same crossing geometry but adjusted for the 1:12 crossing angle studied here, the average dip angle would be 8.5 mrad with most wheels having dip angles between 6 and 12 mrad. A doubling of the average dip angle due to plastic deformation and wear would then mean an average of 17 mrad and some unknown variation. Given these numbers it is assumed that a dip angle range of 6 – 24 mrad is a reasonable range for the present investigation.

Based on the combination of the measured surface geometry of the crossing panel at Loreley and a nominal S1002 wheel profile, the static vertical equilibrium has been solved for each longitudinal position along the crossing. The wheel–rail contact was solved using an implementation of Kalker's algorithm NORM [18]. The vertical wheel trajectory calculated for the measured crossing surface geometry is shown in Figure 9. By numerically evaluating the difference in trajectory slope on the wing rail and the crossing nose close to the transition point, the dip angle at Loreley is found to be approximately 12 mrad.

In [5], a crossing geometry was parameterised both in the lateral (cross-sectional profiles) and longitudinal (longitudinal wing rail and crossing nose inclination) directions. The gauge corner outline and nominal inclinations for wing rail and crossing nose were taken from a standard crossing design of Trafikverket (the Swedish Transport Administration). The cross-sectional rail profiles on the other hand were described using spline functions and were optimised to minimise the contact pressure for a set of measured wheel profiles. Based on this parameterised model, a crossing geometry was created with a crossing angle of 1:12 corresponding to that of the crossing at Loreley. The crossing angle is the angle between the tangents of the through and diverging routes.

The longitudinal inclinations of wing rail and crossing nose are altered for this crossing geometry via vertical height adjustments of the 2D cross-sectional profiles that build up the wing rail and crossing nose, respectively. The magnitude of the vertical adjustment for each cross-section is obtained from linear functions that describe the desired change in longitudinal inclination and vertical position of the wing rail or crossing nose. Here this parameterisation option will be applied to investigate the influence of the crossing's dip angle on the generated impact load and radiated impact noise. The vertical wheel trajectory for cases where the longitudinal inclinations

of wing rail and crossing nose have been modified to achieve different dip angles are presented in Figure 9.

4 Vehicle–track interaction model in the time domain

The prediction method applied in this study includes two separate programs: (1) a time-domain simulation model for dynamic vehicle–turnout interaction and (2) the software TWINS [9] for the prediction of radiated noise.

Vertical dynamic interaction between a wheel and the crossing in the frequency range up to 4 kHz is simulated using a convolution integral approach [19, 20]. This enables a computationally efficient assessment of the dynamic response by calculating the time-variant wheel and rail displacements by a convolution of the vertical wheel–rail contact force with the so-called Green's function of the respective component [21]. A validation of the method is presented in [20]. This was achieved by comparison with a software that previously had been validated versus field measurements. For the track model, Green's functions are derived by a systematic sampling from a set of inverse Fourier transforms of point and cross receptances calculated in a stationary reference frame. As the track model is not periodic, and to account for the motion of the wheel along the crossing, one separate Green's function needs to be calculated for each excitation position along the track. The Green's function for the vehicle model is equivalent with the impulse response function due to radial excitation at the nominal contact point on the wheel. In each time step, an implementation of Kalker's algorithm NORM [18] by Pieringer [22] is applied to solve the vertical non-Hertzian wheel–rail contact. Potential multiple simultaneous contact points occurring for example in the transition of the wheel from wing rail to the crossing nose (and vice versa) are accounted for.

One wheel of the vehicle is modelled as a flexible body suspended in its primary suspension. This vehicle model is considered sufficient since the primary suspension leads to a dynamic decoupling of the unsprung mass from the other vehicle bodies (i.e. bogie frame and car body) at frequencies above approximately 20 Hz [23]. As an example, a BA319 freight wheel with mass 350 kg and nominal rolling radius 0.46 m is modelled using axi-symmetric finite elements, see Figure 11. To obtain the high-frequency modes of the wheel, the hub is first constrained at its inner surface and a modal synthesis is performed retaining a truncated set of eigenmodes corresponding to a highest eigenfrequency of 4 kHz.

Wheelset structural damping is accounted for by introducing a modal damping ratio of 0.001 for all modes. According to experiments, values of structural damping for the wheel eigenmodes are in the range 0.01 – 0.0001 [24]. The value of 0.001 is chosen for practical reasons, although it may be noted that the exact value used for the damping ratio is not critical for rolling noise prediction due to the effective damping introduced by the interaction at the wheel–rail contact [24]. The vertical wheel point mobility corresponding to the vertical velocity at the wheel–rail contact due to a harmonic unit excitation at the same location is shown in Figure 12. The corresponding result for the rigid wheel model is shown for comparison and it will be used later to verify whether a flexible model is needed in the time domain model to calculate impact noise with the equivalent roughness approach.

To account for the load of the vehicle above the primary suspension, a prescribed static displacement of the upper end of the suspension corresponding to an axle load of 20 tonnes is added. In a previous study [12], it was concluded that the influence of the axle load on the generated impact noise levels is low as long as wheel–rail contact is maintained through the crossing.

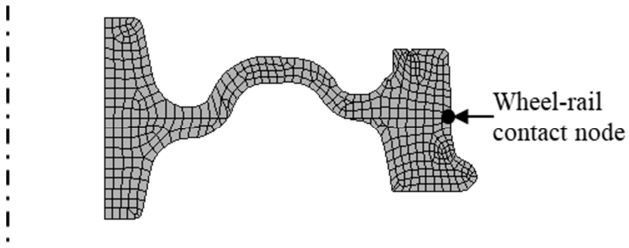

Figure 11. Cross-section of wheel FE-mesh with the prescribed excitation node

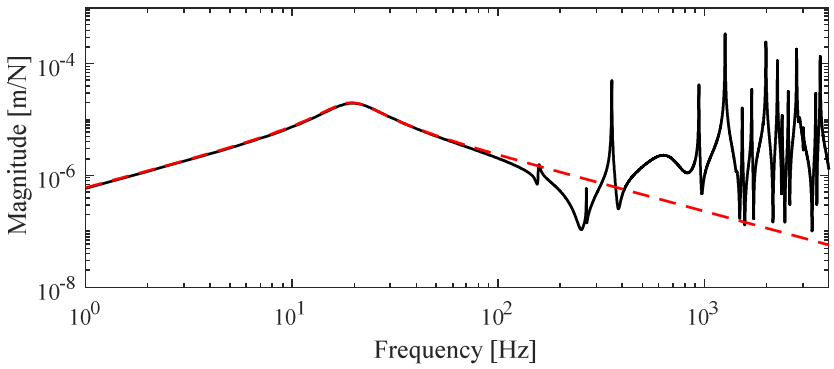

Figure 12. Magnitude of vertical wheel point mobility at the wheel–rail contact node. – – –: Flexible wheel model, —: rigid wheel model

Figure 13(a) shows a sketch of the simplified track model used for the through route in the crossing. It is developed using the finite element method and consists of a discretely supported rail modelled by undamped Rayleigh–Timoshenko beam elements with spatially-varying bending stiffness $EI(x)$, shear stiffness $kGA(x)$, mass per unit beam length $m(x)$ and rotational inertia per unit beam length $mr^2(x)$. At each position x along the crossing, the crossing rail and the two wing rails are combined into one equivalent rail cross-section. Several dimensions, such as thickness, of the hollow rail cross-sections at the Loreley crossing are unknown. For the tuning of the model, based on the outer dimensions of the crossing, the cross-sectional area and moment of inertia over the crossing panel were estimated to vary between four and two times the values for a nominal 60 kg/m rail, see Figure 13(b). This corresponds to a mass distribution varying in the range 240 – 120 kg/m.

To reduce the influence of boundary reflections on the rail vibration at the centre of the model, the track model includes 140 sleeper bays at constant sleeper spacing L = 0.6 m and clamped

boundaries at the two rail ends. The theoretical crossing point (TCP) is located at the centre of the track model directly above sleeper 70. Each rail pad and the support under each (half) sleeper are modelled as two discrete pairs of a linear elastic spring and a viscous damper coupled in parallel. The length and mass M_s of the sleepers are assumed to be constant (150 kg) for sleepers 1 – 60 and 91 – 104. In between, it is assumed that the sleeper length and mass vary linearly from sleeper 61 (150 kg) to sleeper 90 (300 kg). Uniform sleeper support conditions with constant bed modulus are assumed, and thus the linear variation of ballast/subgrade stiffness $k_b(x)$ and damping $c_b(x)$ is proportional to the sleeper length.

The track model was calibrated with respect to the point mobility measured at Loreley. The measurements were performed using sledgehammer excitation of the rail without preload. The measured and calculated vertical point mobilities are compared in Figure 14. On average, the agreement is good. The calibrated track parameters are listed in Table 1. For comparison, the calculated point mobility at midspan when the rail with spatially-varying data has been replaced with a nominal 60 kg/m rail is shown. It is observed that the point mobility on the crossing reveals several peaks and dips that are not commonly found in data obtained from a nominal tangent track. Due to the higher mass and support stiffness in the crossing, the magnitude of the crossing mobility is significantly lower in most of the studied frequency interval. The resonance with low damping at about 1 kHz is the so-called pinned-pinned resonance of the nominal 60 kg/m rail where the wavelength of the vibration is equal to two sleeper spacings. It is observed that this resonance can be identified also in the crossing panel despite the arrangement of rails with varying cross-sections. The procedure for using the Green's function to calculate the vertical rail displacement at the wheel–rail contact is described in [20].

Note that the exact design of the crossing (rail cross-section geometry, mass distribution, etc.) has not been available. Related to this, even though Figure 14 shows a good match between the modelled and measured results, the calibrated track parameters in Table 1 may not correspond to those of the design at the site.

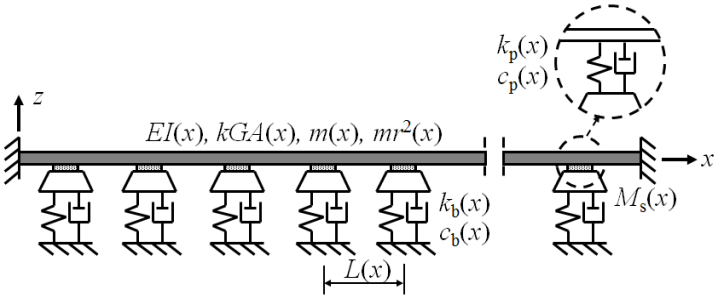

(a)

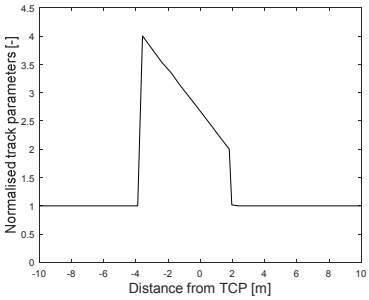

(b)

Figure 13. (a) Track model with one rail on discrete supports. (b) Variation of cross-sectional area $A(x)$ and moment of inertia $I(x)$ for straight rail including the crossing, trailing move; $A(x)$ and $I(x)$ are normalised with respect to $A_{ref} = 7.69 \cdot 10^{-3}$ m^2 and $I_{ref} = 3.05 \cdot 10^{-5}$ m^4 corresponding to a nominal 60 kg/m rail

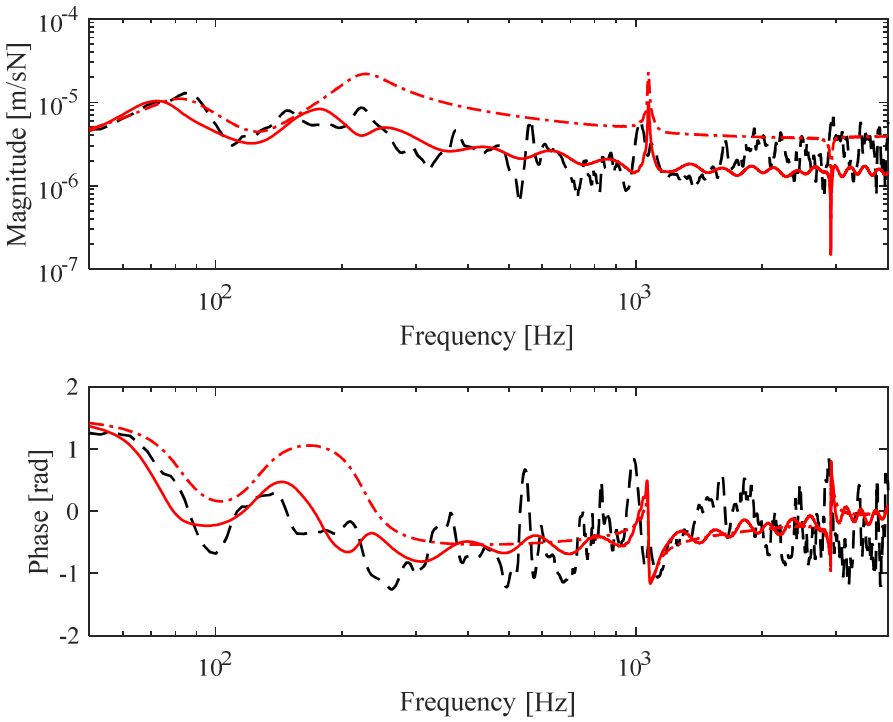

Figure 14. Measured (– – –) and calculated (——) magnitude (top) and phase (bottom) of vertical point mobility at the crossing nose. Comparison with frequency response for nominal rail (– · –)

Table 1. Calibrated nominal parameters of the track support model. The ballast/subgrade stiffness $k_b(x)$ and damping $c_b(x)$ are increased proportionally to the sleeper length in the crossing panel

Parameter	Value
k_p (kN/mm)	60
c_p (Ns/mm)	10
k_b (kN/mm)	50
c_b (Ns/mm)	32.8

5 Wheel–rail impact load

In the simulations of dynamic vehicle–turnout interaction, the continuously varying rail profile geometry along the crossing is accounted for by interpolating the three-dimensional contact geometry between rail profiles given at a sampling distance of 10 mm. The influence of the acoustic roughness, see Figure 8, is neglected. In each time step of the contact detection algorithm, the lateral position of the wheelset centre is prescribed but the contact positions on wheel and rail are not, allowing for an accurate prediction of the wheel transition between wing rail and crossing nose. The effect of variation of lateral contact position on the excitation of wheel and rail is not considered.

Time histories of vertical wheel–rail contact force are simulated for a 10 m long section centred around the TCP, and for traffic in facing and trailing moves. The impact load generated at the crossing by the passage of one wheel is calculated. The influence on the impact load of the different dip angles illustrated in Figure 9 is studied. For a S1002 wheel profile and train speed 100 km/h, the time history of the vertical wheel–rail contact force is shown in Figure 15. It is observed that the impact load magnitude increases with increasing dip angle. For example, the impact load simulated for the dip angle 24 mrad is almost a factor of 2 higher than that obtained for dip angle 12 mrad. Good agreement in impact load magnitude is observed between the measured crossing geometry and the generic geometry with dip angle 12 mrad. This implies that, in terms of the generated impact load magnitude, in the following the Loreley crossing can be represented by the generic crossing with a dip angle of 12 mrad.

An example of the distribution of contact pressure during passage through the crossing panel is illustrated in Figure 16. For a short distance at the transition, there is simultaneous contact on crossing nose and wing rail. The maximum contact pressure is generated at the crossing nose is indicated by the light-yellow colour.

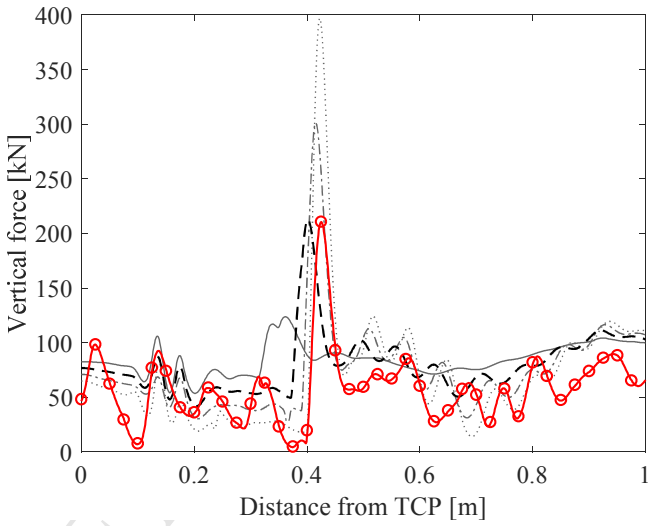

Figure 15. Calculated time history of vertical wheel–rail contact force in the crossing panel. Facing move, axle load 20 tonnes and speed 100 km/h. Results calculated for the pass-by of a S1002 wheel profile on the Loreley crossing (—o—), and on generic crossings with dip angles 6 mrad (——), 12 mrad (– – –), 18 mrad (–·–·–) and 24 mrad (·····)

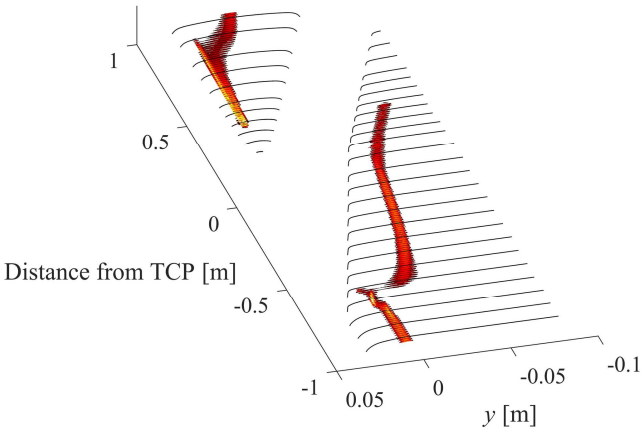

Figure 16. Calculated distribution of vertical wheel–rail normal contact pressure during passage of a BA319 wheel with S1002 wheel profile on the generic crossing with dip angle 12 mrad. Facing move, vehicle speed 160 km/h and axle load 20 tonnes

For an investigation of the influence of flexible and rigid wheel models, calculated time-histories of the vertical wheel–rail contact force during passage through two crossings with dip angles of 12 mrad and 24 mrad are compared in Figures 17(a,b). The contact bands on the wing rail and crossing nose are illustrated on the crossing geometry at the bottom of each figure. For a crossing dip angle of 24 mrad, Figure 17(b) shows loss of contact (zero vertical force) during part of the transition from wing rail to crossing nose. This is illustrated by the simultaneous interruption in the contact bands on wing rail and crossing nose. The influence of the wheel structural flexibility on the impact load magnitude when there is loss of contact is observed in Figure 17(b). The peak force increases by about 40 % but the changes only occur near the discontinuity and for a very short duration.

Time-histories of the vertical wheel–rail contact force for passage through a crossing in facing and trailing moves are compared in Figure 18. Results calculated for dip angles 12 mrad and 24 mrad are presented in Figure 18(a) and Figure 18(b), respectively. It is observed that the impact load magnitude calculated for the trailing move exceeds that for the facing move. This is found to be a consistent observation for a range of vehicle speeds and dip angles, see further results below. It should be noted that these results are obtained for a prescribed lateral wheel–rail shift. To assess the conditions in field would require either measured data for the relative lateral position of the wheel with respect to the rail, or to extend the simulation method to account for the three-dimensional vehicle steering dynamics.

The one-third octave spectra of the wheel–rail contact force based on the output from a simulation over a 10 m section centred at the theoretical crossing point are presented in Figure 19. The results for the two wheel models, and for traffic in the facing and trailing moves, are compared. The frequency components with the largest magnitudes are observed in the low frequency range below approximately 80 Hz. The magnitudes for the rigid wheel model exceed those for the flexible wheel model at most frequencies above 400 Hz, which is where the mobility is lower than that of the flexible wheel, see Figure 12. The difference in the spectra obtained for trains running in facing or trailing moves is seen to be moderate.

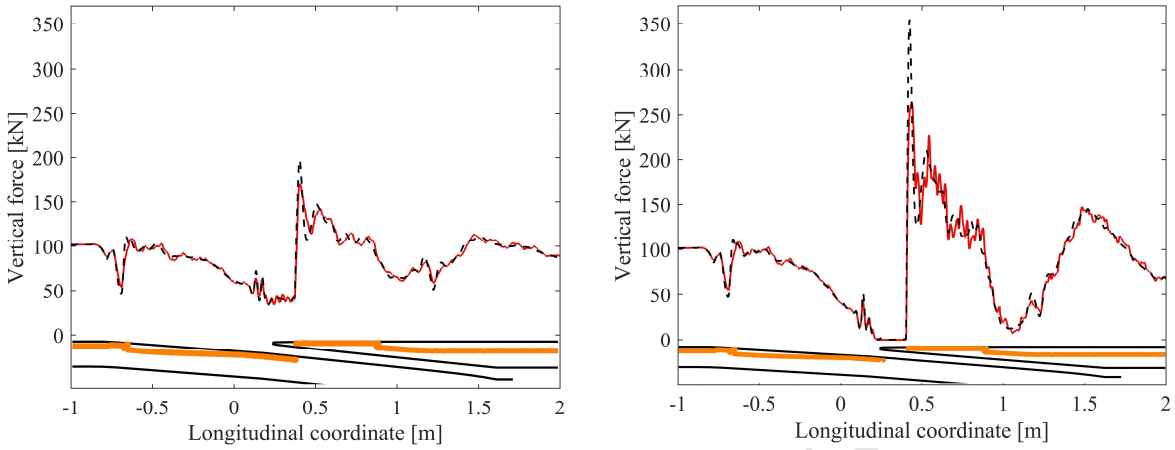

Figure 17. Calculated time-history of vertical wheel–rail contact force for the pass-by of a rigid (– – –) and flexible wheel (—) through the generic crossing with dip angles (a) 12 mrad and (b) 24 mrad. The wheel–rail running band along the crossing is illustrated at the bottom of each figure. Wheel profile S1002, vehicle speed 160 km/h, axle load 20 tonnes and facing move

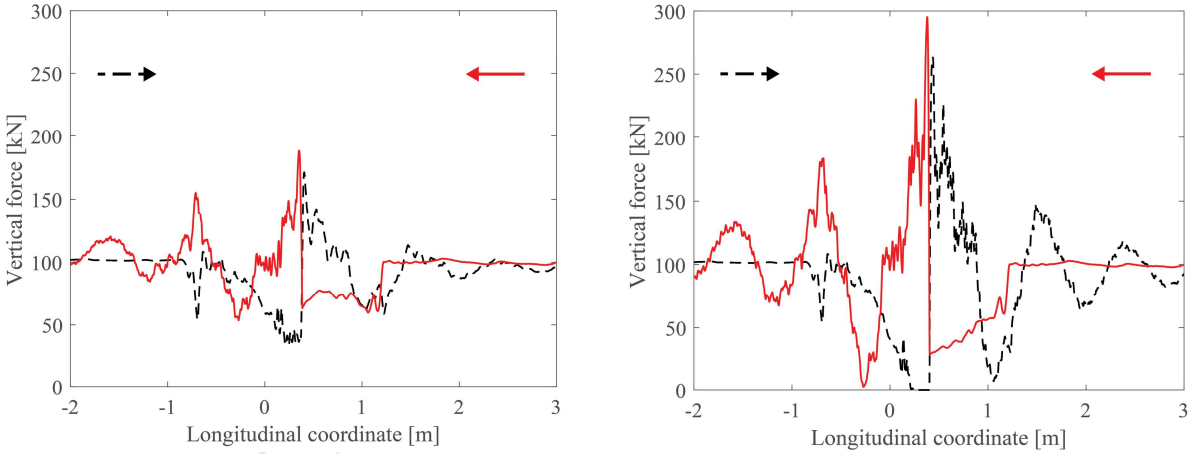

Figure 18. Time-history of vertical wheel–rail contact force calculated for the pass-by of a flexible wheel in facing (– – –) and trailing (—) moves through the generic crossing with dip angles (a) 12 mrad and (b) 24 mrad. Wheel profile S1002, vehicle speed 160 km/h, axle load 20 tonnes. Arrows illustrate the traffic running direction for the respective moves

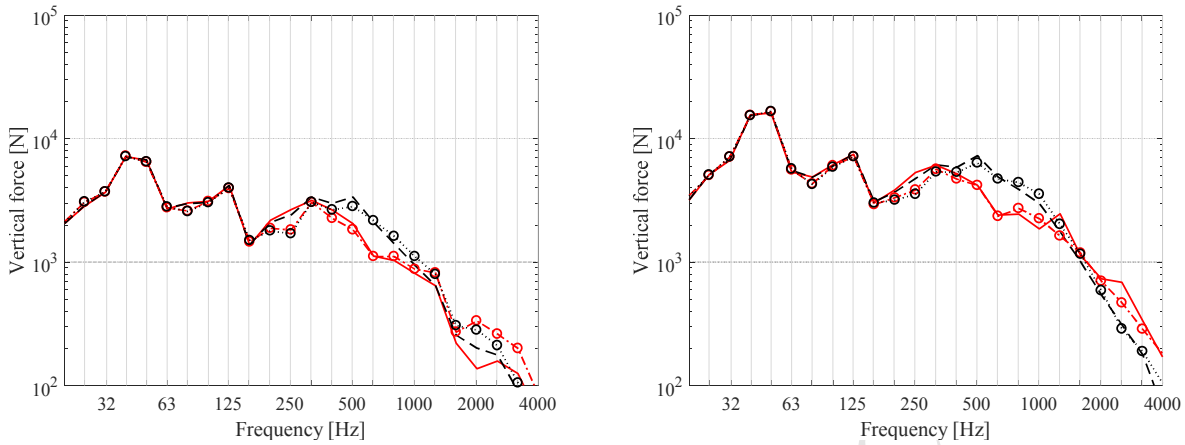

Figure 19. Calculated spectrum of vertical wheel–rail contact force for the pass-by of a wheel with profile S1002 on the generic crossing with dip angle (a) 12 mrad and (b) 24 mrad. Vehicle speed 160 km/h, axle load 20 tonnes and facing move. —: Flexible wheel, facing move; – –: Rigid wheel, facing move; –o–: Flexible wheel, trailing move; ···o···: Rigid wheel, trailing move

A parametric study is performed to investigate the influences of vehicle speed, crossing dip angle and travelling direction on the wheel–rail impact force. Figure 20 presents the ratio of the maximum impact force magnitude to the static vertical wheel–rail contact force. In general, the peak impact force increases with increasing vehicle speed and dip angle, and force magnitudes in the trailing move exceed those in the facing move. A significant difference is seen in the peak magnitudes of the vertical wheel–rail contact force between the results accounting for the wheel structural flexibility and those without. However, cases with loss-of-contact seem not be influenced by wheel flexibility. By comparing the results in Figures 20(a) and 20(c) at dip angle 12 mrad and vehicle speed 180 km/h, the impact load magnitude may be overestimated by approximately 25% if wheel flexibility is neglected. Further, for dip angles 18 mrad and 24 mrad, Figure 20 shows loss of contact to occur at high vehicle speeds. For traffic in the trailing move and dip angle 12 mrad, Figure 20(d) shows that a doubling of speed from 100 km/h to 200 km/h leads to an increase in peak force magnitude by a factor 2. In facing move, the speed dependence of the peak force changes when loss of contact occurs. This can be seen in Figure 20(a) where the peak/static force ratio, for the result at 24 mrad, increases with a slope of about 0.027 per km/h, below 150 km/h. The slope decreases to about 0.015 (per km/h) in the presence of loss of contact above 150 km/h. An equivalent change of slope is not present in the trailing move.

Figure 21(a) illustrates the spectral components of the impact force generated during passage in the facing move at speed 160 km/h and for dip angles between 6 mrad and 24 mrad. The frequency components of the vertical wheel–rail contact force calculated for a dip angle of 12 mrad and vehicle speeds in the range 80 km/h – 240 km/h are presented in Figure 21(b). The spectra in both figures have a similar shape with a maximum force magnitude in the frequency range below 50 Hz. Moreover, the frequency components are found to increase with increasing dip angle and vehicle speed.

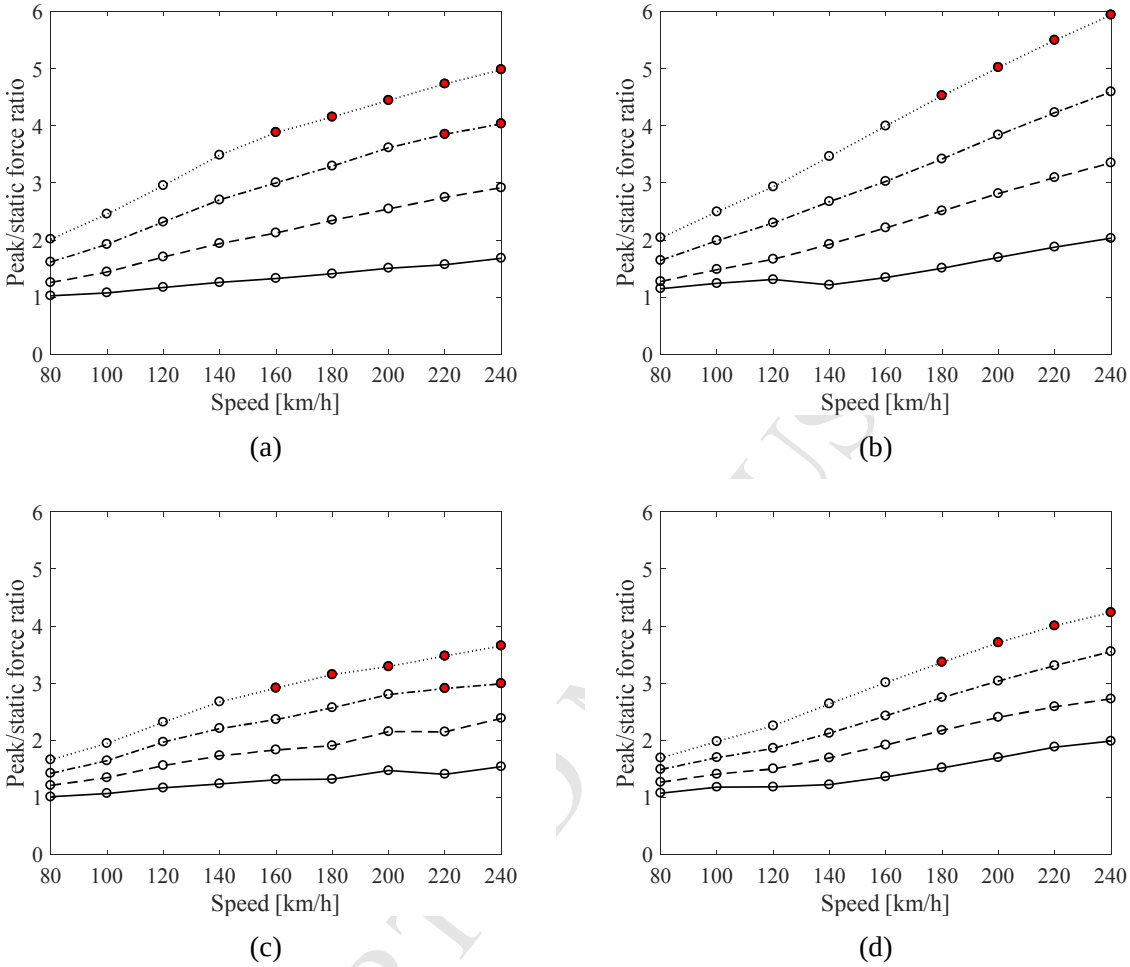

Figure 20. Ratio of the maximum impact force to the static force during pass-by of a wheel through a crossing with dip angles 6 mrad (—o—), 12 mrad (- - o - -), 18 mrad (-·-o-·-) and 24 mrad (···o···). Cases with loss of contact are filled in red. (a) Rigid wheel, facing move, (b) Rigid wheel, trailing move, (c) Flexible wheel, facing move, (d) Flexible wheel, trailing move

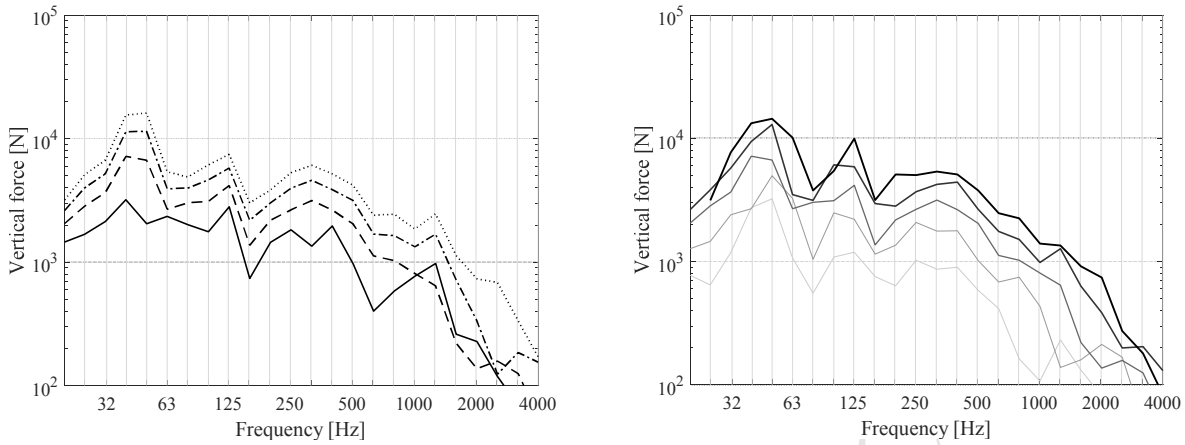

Figure 21. Calculated spectrum of vertical wheel–rail contact force during pass-by of a flexible BA319 wheel with S1002 profile on the generic crossing in facing move. (a) Vehicle speed 160 km/h and dip angles 6 mrad (——), 12 mrad (– – –), 18 mrad (–·–·–) and 24 mrad (·····). (b) Generic crossing with dip angle 12 mrad and vehicle speed varying between 80 km/h (——) and 240 km/h (—) in steps of 20 km/h

6 Equivalent roughness

To estimate impact noise levels from the contact forces calculated in the time domain, a hybrid approach has been developed based on the definition of an "equivalent roughness" [7, 8]. The idea is to determine an equivalent roughness spectrum that, in a linear model, gives the same contact force spectrum as the one obtained with a non-linear model that includes the discontinuity. In this linear model, the dynamic properties of the wheel and track must be the same as in the non-linear time-domain model but the non-linear properties of the contact are replaced by a linear Hertzian contact spring. This roughness spectrum can then be used in a detailed linear model of noise generation, such as TWINS [9], to predict the noise due to the impact. The accuracy of the hybrid approach in predicting the vibration level at the wheel–rail contact point has been quantified in [8] by comparing the velocity spectrum, calculated with this approach, with the equivalent result from a direct integration in the time domain. The maximum difference between the third octave band spectra was less than 2 dB.

The first step is to calculate the transfer function between roughness and contact force for a given combination of wheel type, track and contact. By using a "moving roughness" approach, the contact force per unit roughness can be obtained as

$$H_{rF}(\omega) = \frac{j\omega}{Y_R(\omega) + Y_w(\omega) + Y_c(\omega)} \tag{1}$$

where the denominator includes the sum of rail, wheel and contact mobilities $Y(\omega)$ at circular frequency ω.

The rail mobility is calculated using the track model shown in Figure 13 and the value at the rail discontinuity, where the contact force variations are greatest, is used in Equation (1). The contact mobility is represented by means of a linearized Hertzian contact spring, where the contact stiffness value is calculated from the nominal load and the nominal wheel/rail geometries. The value used in the simulations is 1440 kN/mm. The wheel mobility is the same as shown in Figure 12, and both rigid and flexible models are tested in obtaining the equivalent roughness. These two approaches for the wheel are compared to verify if a model based on a rigid wheel mass can be sufficient to estimate the equivalent roughness.

The contact forces from the non-linear model, see Section 5, are available in the time domain. Typical results are vertical forces (total) as a function of longitudinal position such as those presented in Figures 17 and 18.

To calculate the equivalent roughness, the narrow-band spectrum of the contact force needs to be evaluated. Only the fluctuations of the vertical force around the nominal values result in impact noise, therefore the dynamic fluctuations of F_z are obtained as

$$F_{z,d} = F_z - F_{z0} \tag{2}$$

with F_{z0} being the nominal normal load per wheel ($F_{z0} = 100$ kN). A linear detrend and a steep Tukey window (half-cosines at both ends) are applied to the time histories before calculating the spectrum. These time histories are zero-padded to a length of 2 s and then transformed into the frequency domain, $F(\omega)$, by using a fast Fourier transform. This gives a frequency resolution of 0.5 Hz; the mobilities are also obtained with this frequency resolution. The required equivalent roughness is obtained as

$$r(\omega) = \frac{F(\omega)}{H_{rF}(\omega)} \tag{3}$$

Thus, the force spectra $F(\omega)$ in Equation (3) are obtained from the time-domain model whereas the transfer function $H_{rF}(\omega)$ is obtained from a frequency-domain model. However, it is important that the mobilities used to determine $H_{rF}(\omega)$ correspond to the same track and wheel models used in Section 4 to obtain $F(\omega)$.

The equivalent roughness is finally converted into one-third octave bands to be used in the noise predictions. An example is shown in Figure 22. Note that this roughness corresponds to a time duration of the impact event of 2 s and the noise obtained with using such roughness can be rescaled to be representative of different time windows. In the one-third octave representation of the equivalent roughness, the difference between the rigid and flexible models is negligible in the entire range and for both the cases with and without loss of contact. The mean dB difference is less than 0.2 dB and the maximum difference is 2 dB occurring at the shortest wavelength. Differences in F and H_{rF} cancel out, and this will be reflected in the impact noise. The results found at other speeds and for different dip angles show a similar comparison between the two wheel models. Although the wheelset model (see Figure 17) influences the peak force, a similar effect is not found in the equivalent roughness. This is because in the noise calculations the ratios results shown in Figure 17 need to be converted in dBs, and in addition the equivalent roughness is calculated considering the entire duration of the impact while the wheelset model only affects

the contact force for a short duration. It can therefore be concluded that the rigid wheel model is sufficient in the dynamic simulation once a hybrid approach is adopted to calculate noise. Nevertheless, the wheel flexibility must be included in the calculation of the noise.

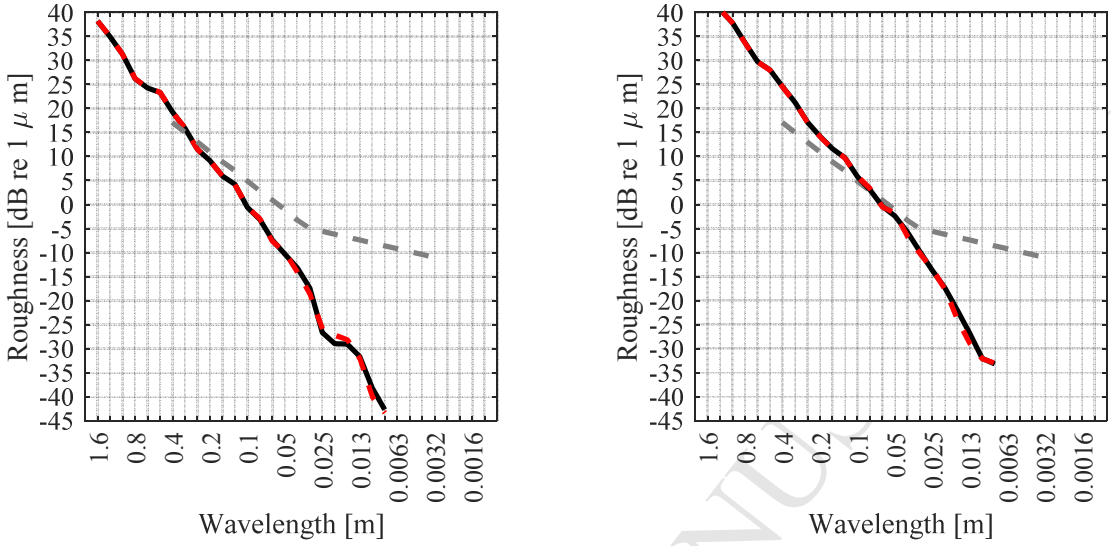

Figure 22. Third octave band equivalent roughness. (a) 12 mrad and (b) 24 mrad. Vehicle speed 160 km/h, axle load 20 tonnes and facing move. Flexible wheel model (——); rigid wheel model (– –); ISO3095 (– –).

7 Impact noise

The software TWINS is adopted to calculate the radiation of impact noise. This model was validated versus field measurements of pass-by rolling noise in Ref. [9]. Additionally, an assessment for the specific application of TWINS as part of a hybrid modelling approach in the prediction of impact noise due to rail joints and wheel flats was presented in [7, 8]. TWINS provides the transfer function between the roughness and the sound pressure at a receiver. For simplicity, the radiation model is based on a nominal rail. For the examples shown below, the receiver is located at 7.5 m from the track centre and at 1.2 m above the top of rail. The roughness-to-pressure transfer function is then combined with the equivalent roughness to obtain a prediction of the noise spectra due to the impact. A contact filter [2] is not included in the noise calculation as this is already directly accounted for in the dynamic simulations presented in Section 5. In the impact noise simulations, only a single wheel is considered and the final results are rescaled to be representative of the spectrum evaluated over a time window of 0.125 s (see also [7]), corresponding to the fast averaging used in acoustic measurements. This corresponds roughly to a travelling distance of 3 m at the lowest speed and 8 m at the highest. For comparison, rolling noise predictions are also evaluated by using roughness measured at the test site as described in Section 2. In the case of rolling noise, the spectra are evaluated over a fixed length of 20 m and include the presence of two axles in each 20 m long car.

The predicted sound spectra are shown for the different cases in Figure 23. All the impact noise spectra (Figure 23(a)-(c)) are characterised by a strong contribution below 500 Hz, while rolling noise spectra (Figure 23(d)) are dominated by frequency bands above 500 Hz. For the rolling noise, with increasing speed the contribution at the higher frequencies increases more than at the lower frequencies. For the impact noise, increasing dip angle results in an increase in noise spectra across the entire frequency range, with only few exceptions at high frequency.

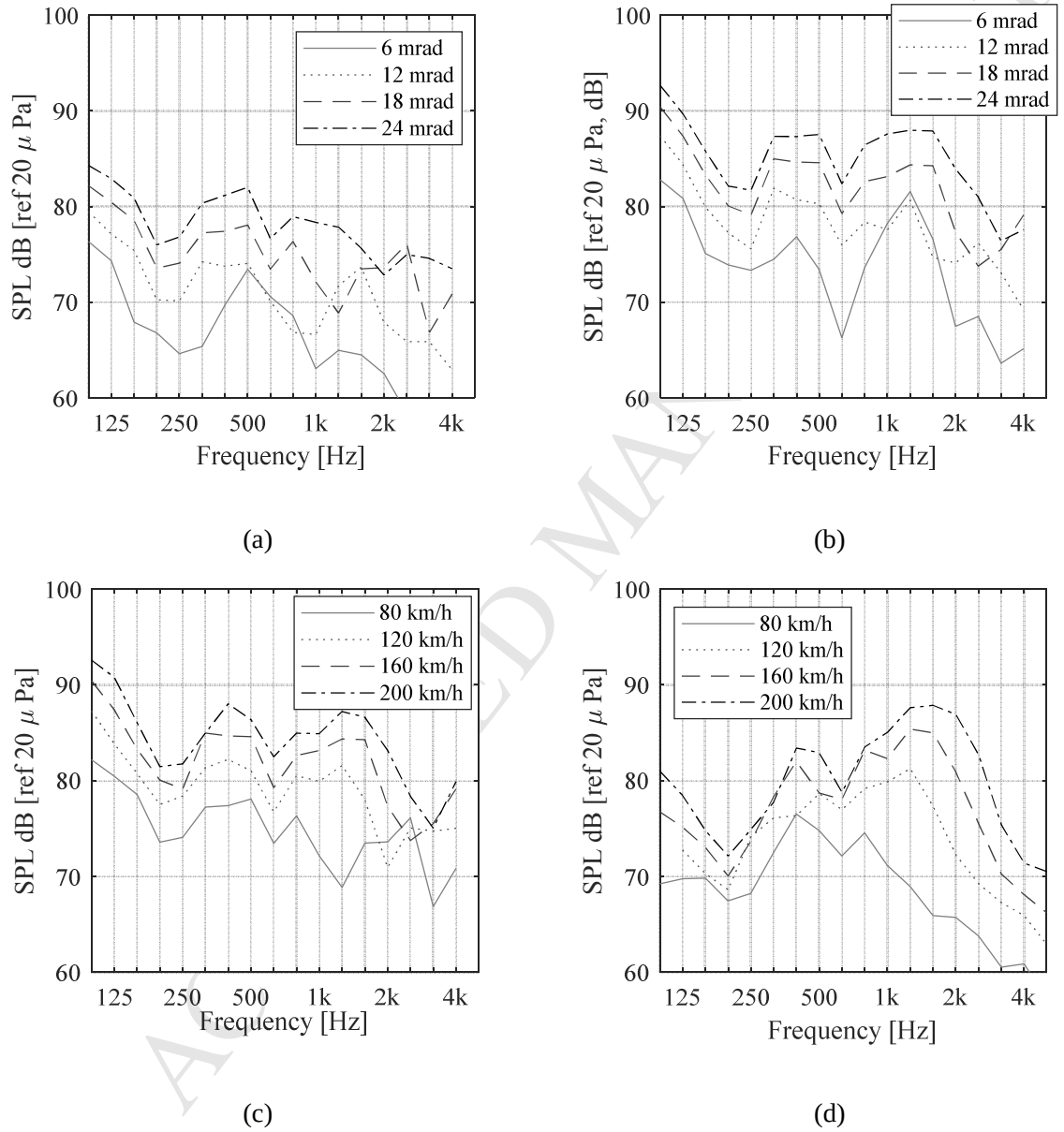

Figure 23. Noise spectra for impact noise and rolling noise simulations at different speeds and dip angles. (a) impact noise at 80 km/h; (b) impact noise at 160 km/h; (c) impact noise at 80 – 200 km/h for 18 mrad dip angle; (d) rolling noise at 80 – 200 km/h

Figure 24 shows the trend of overall A-weighted impact noise level versus speed and compares rolling noise with impact noise at different dip angles. In general, the overall noise level increases with increasing vehicle speed and dip angle. The noise levels in the trailing move are slightly higher than those in the facing move for the cases where there is no loss of contact. However, the difference is on average less than 1 dB. For the dip angles and speed combinations that result in loss of contact the difference is more substantial. As observed for the peak force (see Figure 20), in the facing move the speed dependence clearly decreases when there is loss of contact while it does not change in the trailing move. The facing move shows the type of results attributed in [6] to a step-down impact. In these cases, for speeds where loss of contact occurs, the peak sound pressure was found not to increase with increasing speed. The results for the trailing move instead appear more similar to a step-up type of impact, with the peak sound pressure increasing with increasing speed, regardless of the fact that loss of contact occurs. As a consequence, the overall levels in the trailing move are found to be up to 3 dB higher, for the highest speed and dip angle, than in the facing move. For the cases without loss of contact, the speed dependence of the impact noise is approximately $30 \log V$, which is higher than the $20 \log V$ found in previous research on impact at rail joints [6-8].

It was shown in Figure 9 that the geometry measured at the test site corresponds to a dip angle of 12 mrad. For this dip angle and a vehicle speed of 80 km/h, the overall A-weighted noise level due to a single impact event, evaluated over 0.125 s, is equivalent to the overall rolling noise level (see Figure 24). If the impact noise levels were evaluated over a time window corresponding to a train motion of 20 m, which is equal to the averaging length for rolling noise, the overall level of impact noise would be 7 – 9 dB lower than rolling noise. This is aligned with the observations highlighted through Figures 5 and 6, where it was inferred that the main contribution in the sound pressure spectra is that of rolling noise. However, the impacts are clearly audible in the recorded sound pressure files and intermittently stand out due to their discontinuous nature. Sound spectra averaged over the entire length of a vehicle cannot capture and quantify this effect completely. Evaluating impact noise from S&C with the same time-averaging typical of rolling noise can therefore lead to an underestimate of its actual perceived effect.

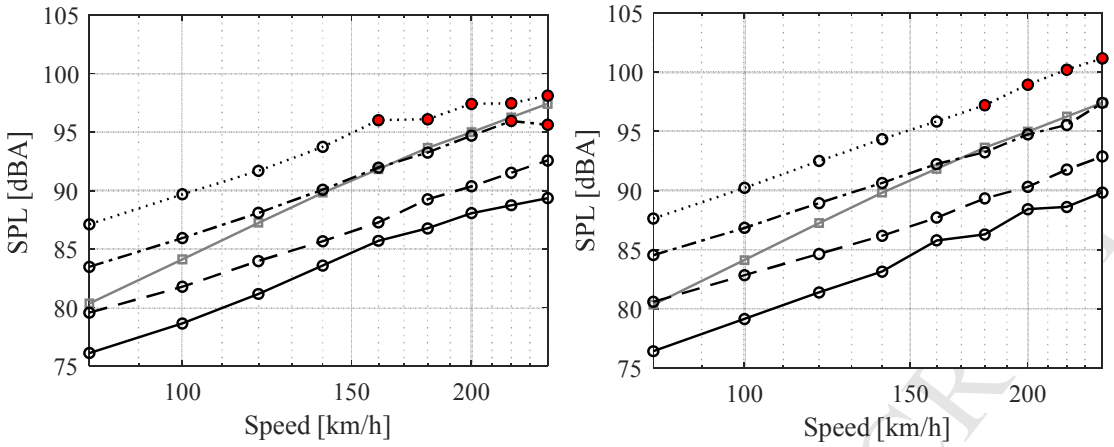

Figure 24. Dip angle 6 mrad (—o—), 12 mrad (- o -), 18 mrad (-·o·-), 24 mrad (···o···) and (—□—) rolling noise. Rolling noise is calculated for a time window corresponding to 20 m, while the impact noise cases are calculated for a time window corresponding to 0.125 s. Cases with loss of contact are filled in red. (a) facing move, (b) trailing move. The *x*-axis is given on a logarithmic scale.

8 Conclusions

Railway crossings are subjected to high degradation rates and hence require regular and expensive maintenance. The large magnitude wheel–rail impact loads generated on the crossing may result in severe plastic deformation and rolling contact fatigue damage that can lead to the breaking out of material from the rails, which in turn brings a further magnification of the impact loads, etc. Another critical consequence of the impact loading is noise. The vehicle speed and the wheel–rail contact geometry, which is determined by the design of the crossing geometry and the status of the wheel and rail profiles, are important parameters with respect to the generation of impact loads and noise. In particular, the magnitude of the impact load is influenced by the crossing dip angle that can be determined from the vertical trajectory of the wheel relative to the rail when passing over the crossing.

In a field test, impact noise and rail acceleration have been measured in a crossing. The point and transfer mobilities measured on the crossing revealed several local maxima and minima not generally found in corresponding transfer functions from standard track. For passenger traffic in the trailing move at speeds in the interval 82 – 87 km/h, the rail acceleration data showed a broad peak centred at 63 – 80 Hz, corresponding to a resonance of the coupled wheel–track system. The measured sound level spectra included the summed contributions of rolling noise and impact noise, and it was not possible to separate them completely. For example, it was observed that the spectra had two significant peaks at 400 and 630 Hz due to rolling noise induced by high rail roughness. The impact noise was observed to influence the low frequency content of the noise spectrum in the region of the wheel-track resonance 63-80 Hz. In general however, it could only be inferred that the contribution of the impact noise to the sound pressure spectra, calculated over a time window corresponding to the length of each passenger coach, was small.

For the prediction of wheel–rail impact loads and noise at railway crossings, a hybrid model has been applied. The hybrid model combines the simulation of vertical wheel–rail contact force in the time domain and the prediction of sound pressure level in the frequency domain. The three-dimensional geometry of the wheel and crossing, and a non-Hertzian wheel–rail contact model, were accounted for in the solution of the wheel–rail contact. The two models are coupled based on the concept of an equivalent roughness spectrum, and it was confirmed that the influence of the crossing dip angle on the impact noise is considerable. For example, an increase in crossing dip angle from 6 mrad to 24 mrad was found to correspond to an increase in radiated impact noise of about 11 dB(A) for the cases without loss of contact. It is concluded that the impact loads and noise can be mitigated by designing for and maintaining a crossing dip angle that is as small as possible. However, since the crossing will be subjected to wheels with different status of wear, a certain dip angle is required for the crossing geometry to be compatible with a range of wheel profile shapes [5, 17]. There are also the hollow worn profiles that typically demonstrate poor compatibility with crossing geometries and induce significant wheel–rail impact loads and rail damage [12].

To the authors knowledge, the current work constitutes a first attempt to use numerical prediction to assess the generation of impact noise at railway crossings. Future research efforts are required to improve the basic understanding of the phenomenon as well as to further develop the simulation method towards a model able to quantitatively validate against field conditions. It is suggested to apply the proposed model to investigate the significance of a field-like spread in operational conditions (e.g. lateral wheel–rail shift and wheel profiles) on the radiation of impact noise. This knowledge may show important for a potential future usage of the model for noise-based condition monitoring. It is argued that the total sound pressure level does not sufficiently well reflect the annoyance experienced by people exposed to impact noise from crossings. Thus, there is a need for a new assessment criterion that accounts for the specific characteristics of impact noise and relates these to other noise sources, such as rolling noise and aerodynamic noise. In order to assess disturbance due to impact noise, such a criterion may need to account for the time-history of sound pressure, evaluate the peak levels and combine these with the number of impacts. These results are currently not predicted with the hybrid approach, which is based on averaged quantities during pass-by.

Acknowledgements

This work was performed as part of the activities in the three-year project IN2RAIL, which started in 2015 and received funding from the European Union's Horizon 2020 research and innovation programme under grant agreement no 635900. Dr. Martin Toward and Mr. Daniel Lurcock of ISVR Consulting at University of Southampton performed and assisted with the analysis of the noise, vibration and rail roughness measurements. Mr. Christophe Muller of Vossloh-Cogifer performed the measurement of the three-dimensional running surface of the crossing panel.

References

[1] W. Grönlund, G. Baumann, INNOTRACK: D3.1.1/D3.1.2 Definition of key parameters and report on cost-drivers for goal-directed innovation (2008), www.innotrack.net

[2] D.J. Thompson, Railway noise and vibration: mechanisms, modelling and means of control, Elsevier, Oxford, UK (2009)

[3] D. Nicklisch, E. Kassa, J.C.O. Nielsen, M. Ekh, S. Iwnicki, Geometry and stiffness optimization for switches and crossings, and simulation of material degradation, Proceedings of the Institution of Mechanical Engineers, Part F: Journal of Rail and Rapid Transit 224 (4) (2010) 279–292

[4] C. Wan, V. Markine, I. Shevtsov, Optimisation of the elastic track properties of turnout crossings, Proceedings of the Institution of Mechanical Engineers, Part F: Journal of Rail and Rapid Transit 230 (2) (2016) 360–373

[5] B.A. Pålsson, Optimisation of railway crossing geometry considering a representative set of wheel profiles, Vehicle System Dynamics 53 (2) (2015) 274–301

[6] I.L. Vér, C.S. Ventres, M.M. Myles, Wheel/rail noise – Part III: Impact noise generation by wheel and rail discontinuities, Journal of Sound and Vibration 46 (3) (1976) 395–417

[7] T.X. Wu, D.J. Thompson, On the impact noise generation due to wheel passing over rail joints, Journal of Sound and Vibration 267 (3) (2003) 485–496

[8] T.X. Wu, D.J. Thompson, A hybrid model for the noise generation due to railway wheel flats, Journal of Sound and Vibration 251 (1) (2002) 115–139

[9] D.J. Thompson, B. Hemsworth, N. Vincent, Experimental validation of the TWINS prediction program for rolling noise, part 1: description of the model and method, Journal of Sound and Vibration, 193 (1) (1996) 123–135

[10] www.creaform3d.com

[11] S.L. Grassie, M.J. Saxon, J.D. Smith, Measurement of longitudinal rail irregularities and criteria for acceptable grinding, Journal of Sound and Vibration 227 (5) (1999) 949–964

[12] P.T. Torstensson, G. Squicciarini, M. Krüger, J.C.O. Nielsen, D.J. Thompson, Hybrid model for prediction of impact noise generated at railway crossings, Notes on Numerical Fluid Mechanics and Multidisciplinary Design, 139 (2018) 759-769

[13] Y. Bezin, I. Grossoni and S. Neves, Impact of wheel shape on the vertical damage of cast crossing panels in turnouts, Proceedings of the 24th Symposium of the International Association for Vehicle System Dynamics (IAVSD) Graz, Austria (2015) 1163-1172

[14] X. Liu, V.L. Markine, H. Wang, I.Y. Shevtsov, Experimental tools for railway crossing condition monitoring, Measurement 129 (2018) 424-435

[15] Z. Wei, A. Núñez, Z. Li, R. Dollevoet, Evaluating degradation at railway crossings using axle box acceleration measurements, Sensors 17 (10) (2017) 2236 (16 pages)

[16] D. Nicklisch, J.C.O. Nielsen, M. Ekh, A. Johansson, B. Pålsson, J.M. Reinecke, A. Zoll, Simulation of wheel–rail contact forces and subsequent material degradation in switches & crossings, Proceedings of the 21st Symposium of the International Association for Vehicle System Dynamics (IAVSD), Stockholm, Sweden (2009) 14 pages

[17] B.A. Pålsson, A linear wheel-crossing interaction model, Proceedings of the Institution of Mechanical Engineers, Part F: Journal of Rail and Rapid Transit 232 (10) (2018) 2431-2443

[18] J.J. Kalker, Three-dimensional elastic bodies in rolling contact, Kluwer academic publishers, Dordrecht, Boston, London (2009)

[19] R. Andersson, P.T. Torstensson, E. Kabo, F. Larsson, An efficient approach to the analysis of rail surface irregularities accounting for dynamic train–track interaction and inelastic deformations, Vehicle System Dynamics 53 (11) (2015) 1667–1685

[20] X. Li, P.T. Torstensson, J.C.O. Nielsen, Simulation of vertical dynamic vehicle–track interaction in a railway crossing using Green's functions, Journal of Sound and Vibration, 410 (2017) 318–329

[21] A. Nordborg, Wheel/rail noise generation due to nonlinear effects and parametric excitation, Journal of the Acoustical Society of America, 111 (4) (2002) 1772–1781

[22] A. Pieringer, A numerical investigation of curve squeal in the case of constant wheel/rail friction, Journal of Sound and Vibration 233 (18) (2014) 4295-4313

[23] K. Knothe, S.L. Grassie, Modelling of railway track and vehicle/track interaction at high frequencies, Vehicle System Dynamics 22 (3-4) (1993) 209–262

[24] C.J.C. Jones, D.J. Thompson, Rolling noise generated by railway wheels with visco-elastic layers, Journal of Sound and Vibration 231 (3) (2000) 779-790